Precise Catalyst Production for Carbon Nanotube Synthesis with Targeted Structure Enrichment

Xiao Zhang, Ying Deng, Brian Graves, Michael De Volder and Adam Boies *

Department of Engineering, University of Cambridge, Cambridge, CB2 1PZ, UK.

* Correspondence: a.boies@eng.cam.ac.uk; Tel.: +44 (0) 1223 746 972.

Abstract: The direct growth of single-walled carbon nanotubes (SWCNTs) with a narrow distribution of diameter or chirality remains elusive despite significant benefits in properties and applications. Nanoparticle catalysts are vital for SWCNT synthesis, but how to precisely manipulate their chemistry, size, concentration, and deposition remains difficult, especially within a continuous production process from the gas-phase. Here, we demonstrate the preparation of W_6Co_7 alloyed nanoparticle catalysts with precisely tunable stoichiometry using electrospray, which remain solid state during SWCNT growth. We also demonstrate continuous production of liquid iron nanoparticles with in-line size selection. With the precise size manipulation of catalysts in the range of 1-5 nm, and a nearly monodisperse distribution ($\sigma_g < 1.2$), an excellent size selection of SWCNT can be achieved. All of the presented techniques show great potential to facilitate the realization of single-chirality SWCNT production.

Keywords: carbon nanotube; catalyst; alloy; nanoparticle; electrospray.

1. Introduction

The rational design and synthesis of nano-catalysts with precisely controlled structures, morphologies, and chemical compositions strongly impact the activity and selectivity of catalysts in applications ranging from the growth of single-walled carbon nanotubes (SWCNTs) to clean energy electrochemical reactions[1] such as the oxygen reduction reaction (ORR), oxygen evolution reaction (OER), or hydrogen evolution reaction (HER). Nevertheless, it is often unachievable to produce nano-catalysts with a targeted diameter, narrow size distribution and specific stoichiometry, particularly if the diameter of the particles is smaller than 5 nm or if the particles should contain alloyed chemistry. These factors especially hinder the growth of SWCNTs with specific chiralities, which is needed for applications such as next generation electronics and optoelectronics[2, 3].

For chemical vapour deposition (CVD) of SWCNTs, alloyed catalysts such as W_6Co_7[4, 5], Co_xMo_y[6] or Co_xNi_y[7] introduced new hope for in-situ enrichment of certain SWCNT chiralities. However, among the reported methods, synthesis of key alloyed catalysts is still restricted by the random nucleation from the colloidal solution[6] and aerosol[7], or use of specific organic molecules[4]. Precisely manipulating the chemistry of every single tiny alloyed nanoparticle (< 5 nm) then becomes critical but difficult, because of the common stoichiometry deviation between catalysts during catalyst nucleation and growth, which can affect the crystalline structure and the uniformity of catalyst performance.

On the other hand, because of the diameter correlation between the SWCNT and catalyst, a chemistry independent method to precisely control catalyst sizes smaller than 2 nm is a long-sought goal. Recently, our group showed the first study to realize the continuous synthesis of solid catalysts (W, Mo and Re based) with a size smaller than 2 nm[8]. These solid catalysts remain in a solid state in the high temperature CNT growth environment. However, although regarded more efficient on catalyzing CNT growth with special enhanced enrichment of near-armchair chiralities, the corresponding continuous synthesis of liquid catalysts (Fe, Ni and Co based) also with precise size

46 manipulation is still missing. Additionally, the size-dependent influence on SWCNTs also needs to
47 be confirmed.
48   Here, we present the first study on the use of electrospray techniques to continuously produce
49 W_6Co_7 alloyed nanoparticles with precisely manipulated stoichiometry and size. On the other hand,
50 we also present a continuous production method for typical liquid catalysts – Fe based nanoparticles
51 – using a straightforward gas-phase synthesis and in-line size selection techniques. This allows for
52 precisely manipulated size to any target value in the region of 1-8 nm and a narrow size distribution.
53 The constraint effect on the diameter of SWCNTs (d_t) can be clearly seen. These new advances are
54 important to develop future continuous synthesis methods for chirality controlled SWCNTs.

2. Results

2.1. Production of Alloyed Naono-Catalysts and their growth of CNTs

2.1.1 Nanoparticle Production from Electrospray Method with Precise Stoichiometry

58   With W-Co alloyed catalysts as an example, synthesis begins with the generation of gas-phase
59 W-Co compound salt nanoparticles (sNPs) suspended in a carrier gas as shown in Figure 1. With the
60 gas-phase transport, sNPs pass through size-selection and controlled deposition. The W-Co alloyed
61 catalyst (Refractory-Ferromagnet metal alloyed catalyst) is a typical solid catalyst to support the
62 growth of SWCNTs, which remain rigid and crystalline in a CNT growth environment, believed to
63 strongly affect the chirality enrichment in the final product [4, 6].

64
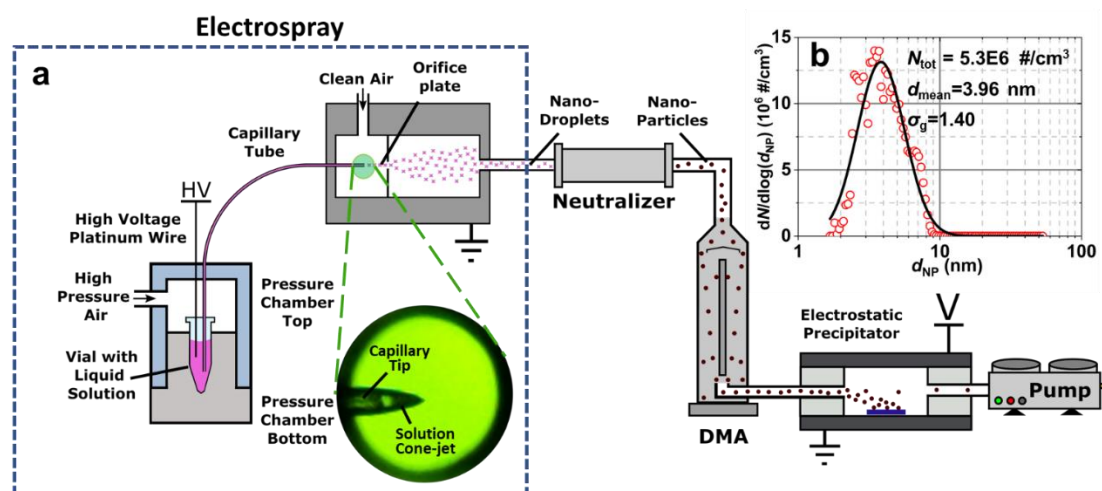
Figure 1. Experimental setup schematic for the continuous W_xCo_y alloy nanoparticle generation, size selection and collection. The mixed solution of W and Co based compound solution were cone-jetted into nano-droplets by the electrospray aerosol generator (**a**), due to the high electric field between solution cone and orifice plate. After the highly charged nano-droplets are neutralized and self-dried after passing through the neutralizer, W-Co salt nanoparticles form but with a polydisperse size distribution as characterized by a Scanning Mobility Particle Spectrometer (**b**) with diameter range within 1-10 nm, and geometric mean particle diameter (d_{mean}) ~3.96 nm, geometric standard deviations (σ_g) ~1.4, and concentration (N_{tot}) of 5.3×10^6 #/cm^3. They are further size selected by a Differential Mobility Analyzer (DMA) and deposited onto the substrate in an electrostatic precipitator.

75   As shown in Figure 1a, the mixed solution of W and Co based compounds passes through a
76 capillary tube driven by the high gas pressure. Under optimized parameters, the solution cone
77 formed at the tip of capillary facilitates the jet of nano-droplets driven by the high voltage difference
78 between the cone and the orifice plate. The jetted highly charged nano-droplets are timely neutralized
79 and self-dried in the carrier gas, forming the sNPs.

80　　　The size distributions of sNPs are first characterized by a Scanning Mobility Particle
81　Spectrometer (SMPS) (Figure 1b). Owing to the nanoscale of the droplet jet, the nanoparticles (sNPs)
82　formed after solvent removal is well constrained to < 8 nm with mean diameter (d_{mean}) ~3.96 nm, which
83　is much smaller than sNPs formed by a common atomizer (>10 nm)[8, 9].
84　　　After constraining the sNP size with cone-jetting, the size distributions of the sNPs are further
85　narrowed by a Differential Mobility Analyzer (DMA). In the following section of this work, (for liquid
86　catalysts), the size selection principle of the DMA will be illustrated in detail. With final controlled
87　disposition onto various target substrates by an electrostatic precipitator, sNPs are evenly distributed
88　on the collection zone with a tunable areal density (Figure 2a). The size distribution of selected NPs
89　follows the log-normal distribution with geometric standard deviation (σ_g) to be 1.21 based on AFM
90　statistics, much smaller than the that before DMA size selection (σ_g=1.40). σ_g can be further lowered
91　to 1.05 based on our previous research[8] as long as the aerosol concentration is high enough to
92　guarantee efficient collection.

93
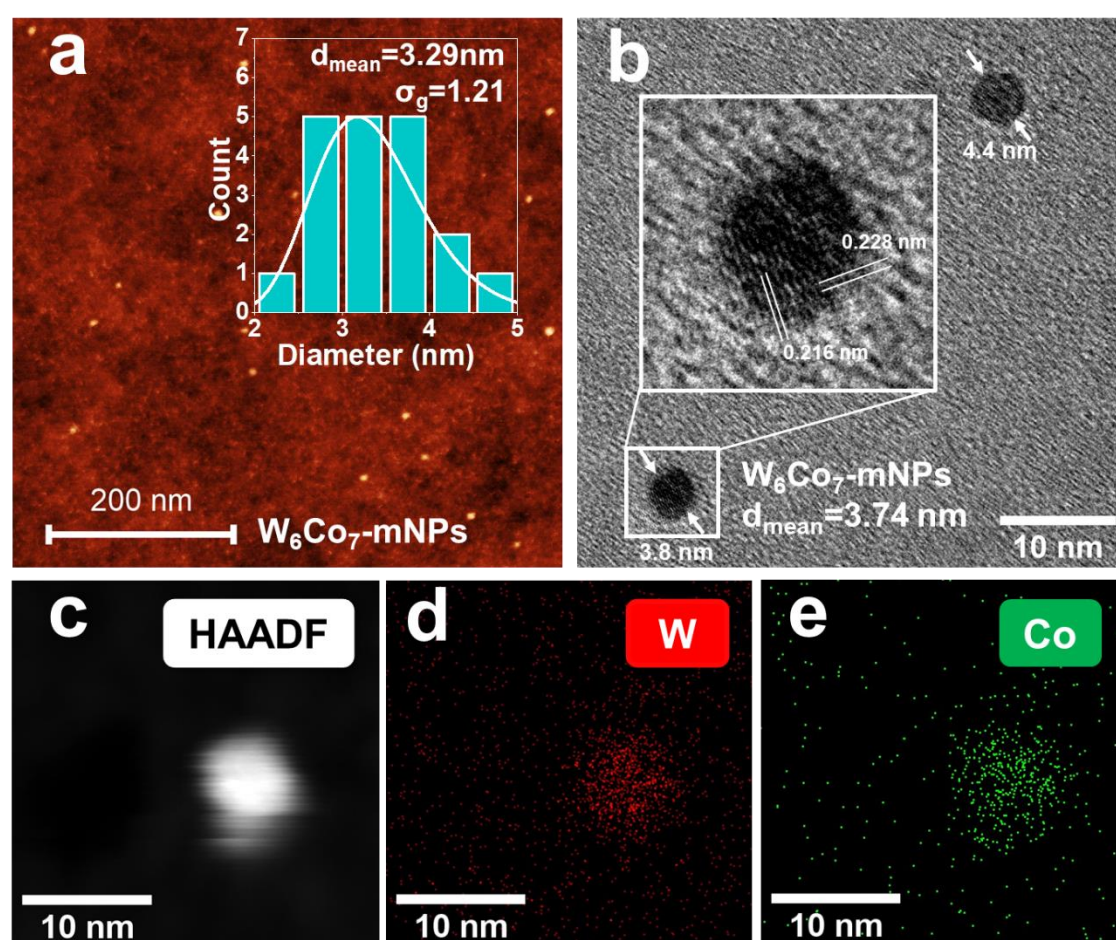
94　　　**Figure 2. Nanoparticles after size selection and their crystal structure determination.** (**a**) AFM
95　images of size selected W-Co sNPs homogeneously deposited on SiO_2/Si substrates. Particle
96　populations possessing narrow size distributions (σ_g = 1.21) with small mean diameters (d_{mean}=3.29
97　nm) are shown in the inset histogram. Also shown is HRTEM image (**b**) of single crystal W-Co alloy
98　mNPs after reduction and reconstruction. d_{mean}=3.74 nm is measured by AFM not shown (**c-e**) With
99　the Energy-dispersive X-ray spectroscopy (EDS) elements mapping on single W-Co mNPs, (**c**)
100　Scanning transmission electron microscopy (STEM) image acquired using the High angle annular
101　dark field (HAADF) detector is shown with the EDX spectra/maps on both (**d**) W and (**e**) Co. Both
102　elements distribute uniformly across the single crystal mNPs instead of the combination of multi-
103　crystals. No accumulation of oxygen element is seen in the area of NP, verifying the alloy metal state
104　of the NP, mNPs.

105   After calcination and reduction at high temperature in H_2, the sNPs are reconstructed into single-
106   crystal alloyed NPs (alloyed-mNPs, Figure 2b-e). Based on our previous work, the diameter is
107   observed to shrink by ~40% (60% remaining) during this process after losing of O, N, and H and
108   reconstruction[8]. Energy-dispersive X-ray spectroscopy (EDS) elements mapping verifies that both
109   W and Co elements are uniformly distributed across the alloyed-mNPs. The atomic ratio of W:Co
110   measured by EDS is (42.3±7.1) : (57.8±8.3). Combined with the interplanar distances of mNPs
111   measured from HRTEM, our particles' characteristics are in good agreement with those of W_6Co_7
112   (PDF exp.2-1091). Figure 2b inset shows interplanar distances 0.216 and 0.228 nm of the (1 0 10) planes
113   and (1 1 3) in W_6Co_7 alloyed, respectively. Moreover, no accumulation of oxygen is seen in the area
114   of the NP, verifying the alloyed metal state of the NP. We suggest the alloyed-mNPs are W_6Co_7
115   alloyed single crystals (details of the crystal structure identification can be found in supplementary
116   material).
117   Importantly, with this electrospray method, each nanoparticle is formed from one nano-droplet,
118   thus the stoichiometry of the sNPs and mNPs are precisely equal to that the solution from which the
119   nano-droplets are formed. Here, the atomic ratio of W:Co in the prepared mixed solution is 6:7, match
120   the stoichiometry of W_6Co_7 catalysts and the EDS results.

121   2.1.2. CNTs Grown from the Alloyed Nano-catalysts

122   The NPs produced in this work are based on a continuous gas-phase process. In our previous
123   work, we demonstrated its potential to be extend into a floating catalyst CVD process (FCCVD)[8].
124   However, for the sake of convenience, and a better control on the synthesis parameters of NPs and
125   CNTs, all the CNTs in this work are gown using a batch process from substrates loaded by produced
126   NPs.
127   Due to the gas-phase nature of the sNPs formation process, by modifying the receiving target
128   substrates, CNTs can be facilely grown on various targets without any ex-situ transfer processes.
129   Figure 3 shows random CNTs grown on SiO_2/Si (Figure 3a) and aligned array (Figure 3b) on ST-cut
130   quartz substrate because of the guidance from the atom steps of the substrate[10]. By decoupling the
131   catalyst size from their areal density, further growth of high density SWNT arrays for electronics
132   becomes possible[11, 12]. Moreover, it is worth noting that, in SEM images of CNTs laying on
133   insulating substrate (SiO_2/Si) obtained with low accelerating voltage (1-3 kV), the bright line in images
134   (Fig.3a-b) originates from not only the CNT itself, but also from the adjacent zone of substrate affected
135   by the CNT[23]. Therefore, the diameter of bright lines cannot represent those of CNTs.

136
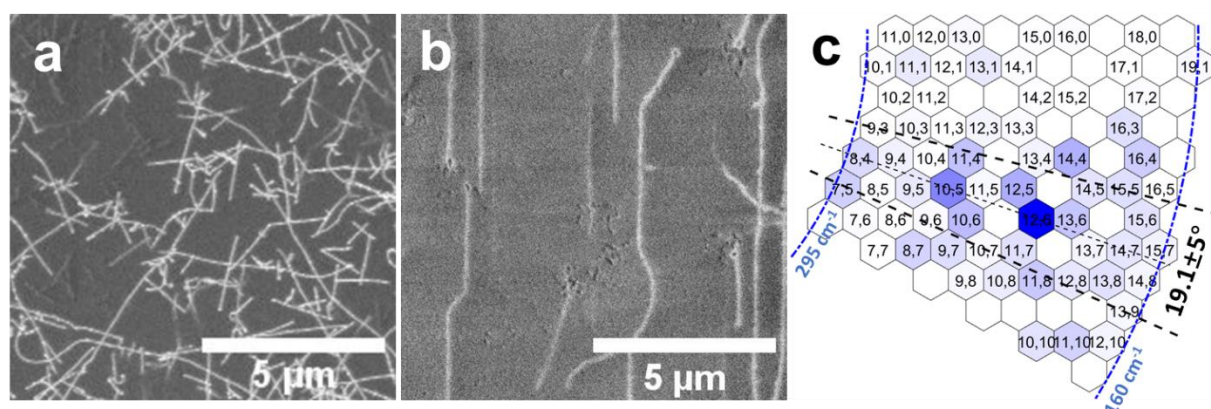
137   **Figure 3. CNTs grown from W-Co alloy nano-catalysts. (a)** Random and **(b)** aligned CNT array
138   grown on SiO_2/Si and ST-cut quartz substrates without any ex-situ transfer processes. **(c)**Chirality
139   enrichment is measured by Raman RBM with 532, 638 and 785 nm lasers on random CNTs arrays
140   grown on the SiO_2/Si substrate. The peak position abundance statistics results from three lasers are
141   summarized with normalized scale. After converting peak position abundance to chirality abundance
142   based on the Kataura Plot, the results are displayed on map. To guarantee unambiguous
143   identification, the painting is done only for SWCNTs with 0.81 nm < diameter < 1.53 nm (160-295 cm-

144   [1], marked by the blue dash-dotted line). Chirality cells that are not resonant with three lasers are left
145   empty. Chiralities near $(2n,n)$ most enriched (corresponding range of 19.1±5° are marked by a black
146   dashed line), and few can be found near the zigzag region.

147   With RBM (radial breathing mode) peaks from Resonant Raman spectroscopy of SWCNTs
148   detected with 532, 638 and 785 nm lasers, the chiralities abundances are identified based on Kataura
149   Plot and summarized in graphene map (Figure 3c). To guarantee unambiguous identification, the
150   colour density is indicative of solely SWCNTs within 0.81-1.53 nm (160-295 cm^{-1}, marked by the blue
151   dash-dotted line). Chiralities near $(2n,n)$ most enriched (corresponding range of 19.1±5°) are marked
152   by a black dashed line, and few can be found near the zigzag region. The most enriched visible
153   chiralities are (12,6), (10,5), (13,6) and (12,5), which are all on or near $(2n,n)$, with chiral angle near
154   19.1°. This result matches the solid catalysts performance we reported recently[8]. The highest
155   abundance of (12,6) reached approximately 22% among the diameter range of 0.81 – 1.53 nm. The
156   slightly lower abundance compared with previous report is mainly because of the comparatively
157   larger size of W-Co alloyed catalyst currently with electrospray method, which is a compromise to
158   reach higher catalyst production rate and collection efficiency. Currently, the yield of our electrospray
159   method is around 10^1-10^3 #/cm^3/min, which set up many difficulties on characterization and size
160   selection. However, significant advancements in electrospray have been made in recent years as a
161   part of a large effort by the synthesis community[24]. The yield can also be improved in the future by
162   using the electrospray with multi cone-jets, instead of a single one used here. Considering the unique
163   advantage of electrospray method on the manipulation of stoichiometry in the nano-catalyst, further
164   work could effectively reduce the size of alloyed catalyst and further constrain chiralities.

165   *2.2. Production of Size-manipulated Fe-based Catalyst and the SWCNTs Diameter Constraint*

166   2.2.1. Fe$_2$O$_3$ Nanoparticle Production with Precise Size Manipulation

167   For liquid iron catalyst, we follow our reported techniques[8] to produce the metal-oxide
168   nanoparticles (oNPs) in the gas-phase. Then to grow SWCNTs, the Fe-oNPs are reduced into Fe metal
169   nanoparticles (Fe-mNPs), forming the final catalyst upon the supply of carbon feedstock. As shown
170   in Figure 4, the ferrocene vapor taken by carrier air gas enters the high temperature furnace (700℃),
171   calcinated into Fe-oNPs. The dominant sizes of Fe oNPs are adjustable from 2 to 10 nm by varying
172   the input of Fe precursor input (temperature of ferrocene container and the flow rate of carrier air
173   gas).

174
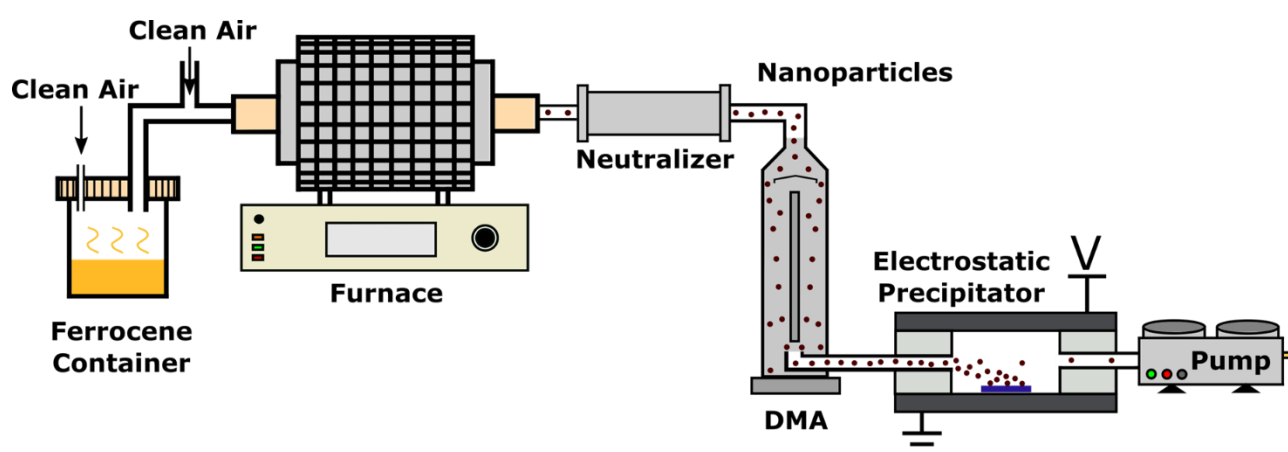
175   **Figure 4. Experimental setup schematic for the continuous Fe$_2$O$_3$ nanoparticle generation, size
176   selection and collection.** The ferrocene vapor is carried by particle-free air and enters the tube furnace
177   set to 700℃, where the ferrocene is calcined into Fe$_2$O$_3$ nanoparticle (Fe-oNPs) and flow to the
178   downstream. After being charged by a neutralizer, the polydisperse Fe-oNPs are size-selected by
179   DMA, and finally deposited onto a substrate in the electrostatic precipitator.

180   Although small and highly concentrated, Fe-oNPs' size is still too broadly distributed to
181 effectively constrain the diameter of SWCNTs. Similar to the techniques above, proactive NP mobility
182 selection is integrated into the mainstream to transform the distribution of entire aerosol flow from
183 polydisperse to monodisperse. In this process, after being charged by a radioactive ionizer, the oNPs
184 are passed between two concentric cylinders in the DMA at an electrical potential difference. Only
185 oNPs with prescribed mobility-equivalent diameter pass downstream, which results in the narrow
186 size distribution of selected Fe-oNPs.
187   Using AFM, the size distribution of these selected Fe NPs are measured (Figure 5a-d). Their sizes
188 are precisely tuned in the range of 1 to 8 nm. From relatively large Fe-oNPs (Figure 5a), it is obvious
189 that the as-produced Fe-oNPs are nanoaggregates with irregular morphologies. After being
190 processed in H2 at 400℃, the nanoaggregates are reduced and reconstructed into rounded NPs (and
191 inevitably re-oxidized in the air when characterized by AFM). Meanwhile, for all sizes, the size
192 distribution after selection is inherited to that of NPs after reduction and reconstruction (Figure 5a-
193 d, σ_g ~1.2, and σ_g =1 represents ideal monodisperse particles). This implies that processing in H_2 at
194 400℃ for 5 mins will not broaden the size distribution although the aggregation and Ostwald
195 ripening effect are enhanced.

196
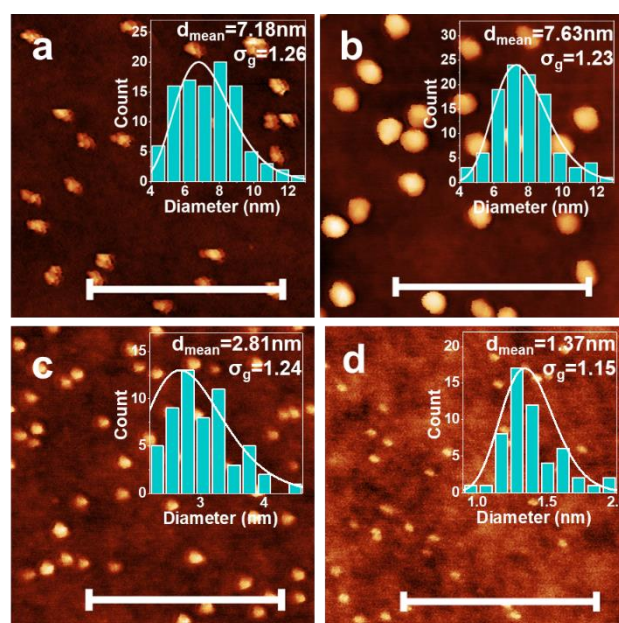
197   **Figure 5. AFM images of Fe Nanoparticles after size manipulation.** (**a**) 7.18 nm Fe_2O_3
198   nanoaggregates homogenously deposited on SiO_2/Si substrates. (b) After reduction and
199   reconstruction under 400 ℃ in H_2, the irregular Fe_2O_3 nanoaggregates become more rounded
200   (oxidized again in air because of AFM characterization) without size distribution degraded. With
201   other size selection, the Fe nanoparticles are precisely manipulated to obtain (**c**) 2.81 nm and (**d**) 1.37
202   nm Fe-oNPs. All possessing narrow size distributions, geometric standard deviation σ_g ~1.2.
203   Moreover, smaller the d_{mean}, smaller the absolute FWHM for the distribution. Scale bars are all 200
204   nm.

205   It is also worth noting that the absolute FWHM of these selected distributions scales with the
206 selected midpoint size. Therefore, the selection of smaller diameter particles also corresponds to a
207 smaller FWHM (insets of Figure 5b-d, FWHM decreases from 3 to 0.5 nm when d_{mean} decreases from
208 7.6 to 1.4 nm). This is the key feature for achieving nearly monodisperse Fe catalysts for SWCNT
209 growth.

210   2.2.2. Constrain SWCNTs Diameter by Fe Catalysts

211   In Figure 6, we compared the diameter distribution of SWCNTs grown from size-selected 1,8
212 nm (Figure 6 a–i) and 3.6 nm (Figure 6 j–l) Fe-oNPs catalysts. Resonant Raman spectroscopy shows

213   the RBM peaks of SWCNTs in the laser spot excited with laser phonons[3, 13]. We follow our reported
214   method[8] on Raman mapping characterization and data analysis. In Figure 6 a-c, we show the raw
215   Raman spectra of 1.8 nm Fe-oNPs on RBM region detected by 532, 638, and 785 nm lasers.
216   The peak position of each spectrum is identified after background removal (SiO₂/Si signal, Figure
217   6 d–f). Based on RBM peaks frequency (ω_{RBM}) to the diameter of SWCNT (d_t) relationship for samples
218   grown on SiO₂/Si substrates[14], $\omega_{RBM} = 235.9/d_t + 5.5$, we obtain the diameter distribution statistics
219   from the peak position abundance statistics results (Figure 6 g-l).

220
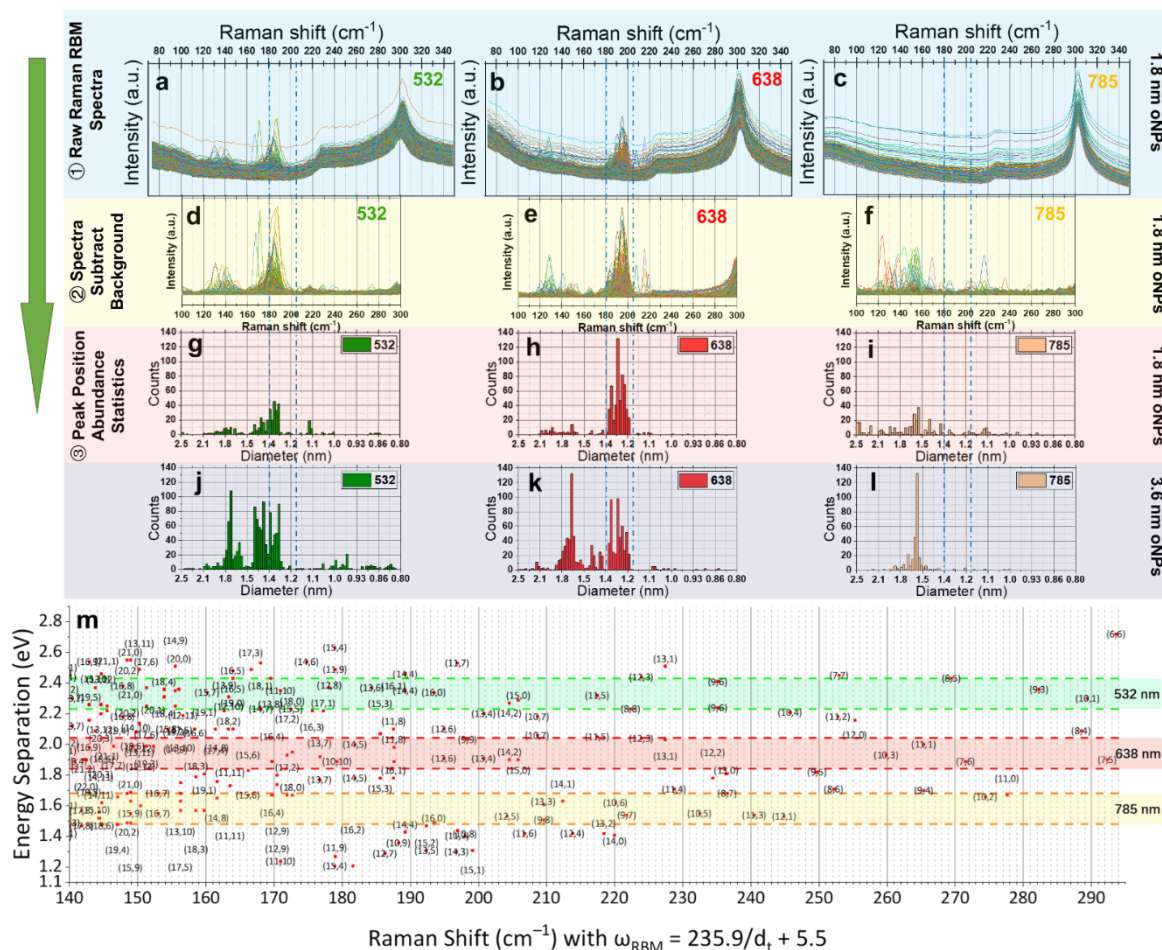
Figure 6. The comparison between constraint effects on the diameter of SWCNTs grown from Fe
catalysts with different sizes. (a–c) Raw Raman spectra at RBM region (70–350 cm⁻¹) of SWCNTs
grown from 1.8 nm Fe-oNPs detected by 532, 638, and 785 nm lasers. (d-f) The peak position of each
spectrum is identified after background removal (SiO₂/Si signal). The spectra tails around 290-300 cm⁻¹
are generated during background removal; (g–i) For SWCNTs grown from 1.8 nm Fe-oNPs, the
peak position abundance statistics obtained by different lasers are normalized by pixel number and
laser spot area. (j–l) For SWCNTs grown from 3.6 nm Fe-oNPs, the normalized peak position
abundance statistics. (m) Modified Kataura plot is used to identify the resonant chiralities. Regions of
diameter from 1.18–1.4 nm are marked by dash-dotted lines.

230   Here, with Raman $x-y$ 2D mapping results from 532, 638, and 785 nm lasers, respectively, the
231   resonant peak position abundance statistics results are summarized with a normalized scale so that
232   peak counts can be compared between different lasers. However, as is well known, the scale of
233   detectable SWCNTs in each Raman mapping result depends on both diameter distribution of the
234   sample and whether resonance happens with the laser wavelength, according to Kataura Plot[15, 16],
235   as shown in Figure 6 m.
236   In our results, for abundance detected by 638 nm laser (Figure 6 h vs k), it is clear that 1.8 nm Fe-
237   oNPs catalysts preferentially produce more 1.2-1.4 nm SWCNTs and fewer for d_t >1.4nm.

238   A similar trend can also be seen by 532 nm laser (Figure 6 g vs j), SWCNTs with d_t >1.4 nm is
239   much suppressed with 1.8 nm Fe-oNPs catalysts, although $1.2 < d_t < 1.3$ nm cannot be detected by 532
240   nm laser because of a lack of resonance and the known bias of the chirality distribution to the
241   armchair chiralities with liquid catalysts like Fe[17].
242   For 785 nm laser results(Figure 6 i vs l), the disappearance of 1.2-1.4 nm SWCNT enrichment is
243   also due to the poor resonance condition and the chirality distribution propensity for armchair
244   chiralities. The suppressed abundance peak around 1.6 nm tends to verify the constraint effect from
245   the size of catalysts.

3. Discussion

247   To pursue single chirality SWCNT growth, the mechanisms underlying the chirality selection of
248   SWCNTs are of great importance. However, many theoretical contributions have been proposed, but
249   always lack sound experimental verification. Among them, interface energy driven nucleation
250   thermodynamics[18-20] combined with CNT growth kinetics[18], as well as the catalyst epitaxy with
251   symmetry matching[4, 21, 22] are the most favorable directions.
252   Before the realization of chirality enrichment, normally specific diameter enrichment in SWCNT
253   product is the precondition. However, not all the grown SWCNTs possess diameters match that of
254   their catalysts, which is known as tangential growth ($d_t \sim d_{catalyst}$). Sometimes, the diameter of a grown
255   SWCNT can be smaller than that of its catalyst ($d_t < d_{catalyst}$), and this is known as perpendicular
256   growth.
257   With in-line size selection using a DMA, we can directly select small diameter catalysts.
258   Although CNT growth is not fixed to either perpendicular growth or tangential growth, small
259   catalysts provide a limited upper bound to the diameter of CNTs regardless of the growth mode.
260   Here, we verified, with 1.8 nm Fe-oNPs that the diameter of SWCNTs can be enriched < 1.4 nm.
261   Consequently, the resultant chirality choices are significantly reduced. Further, combined with the
262   declined chiral angle distribution, the chirality choices are again reduced.
263   The SWCNT diameter distribution results from 1.8 nm Fe-oNPs also implies that the size
264   distribution of catalysts set by NP mobility size selection can still be inherited by SWCNTs, even
265   though Fe is believed to remain in a liquid state during CNT growth and led to more aggregation
266   and Ostwald ripening than solid catalysts.
267   With the electrospray technique, owing to its chemistry-independent property, as long as mixed
268   solutions of corresponding soluble compounds are prepared, similar alloyed catalysts such as Mo-
269   Fe, W-Fe, Re-Ni etc. can also be produced with precise manipulation of stoichiometry.
270   Further, combined with proper processing, the formed single crystal nano-catalyst with different
271   chemistry and stoichiometry give researchers, for the first time, an ability to manipulate the interface
272   between CNT and catalyst, where the interfacial energy has been reported to determine the chiral
273   preference of SWCNTs by affecting the possibility of nucleation, the growth speed and even the
274   growth time.

4. Conclusions

276   With the mechanism of one nanoparticle formed from one atomized droplet, we produce W_6Co_7
277   alloyed nanoparticles successfully with the same target chemistry in a continuous gas-phase method.
278   They act as the solid catalyst to grow SWCNTs with chirality control. As an example, for liquid
279   catalysts, we produce the gas-phase size-selected Fe based nanoparticles with a size down to 1.5-1.8
280   nm. The small diameter of these liquid catalysts shows an obvious diameter constraint effect on
281   SWCNTs, with diameter highly enriched < 1.4 nm.
282   We assert that the two techniques shown here can be used to provide a useful set of experimental
283   designs to support or rule out potential theoretical mechanisms, facilitating measuring the physical
284   parameters, finally forming a cohesive and useful theory that can guide the development of models,
285   experiments and production of chirality-controlled CNTs.

5. Materials and Methods

5.1. Nanoparticle Synthesis, Size Selection, and Collection

Production of alloyed W_6Co_7-nanoparticles: An aqueous mixed metal salt solution is prepared with 25 μM $(NH_4)_6H_2W_{12}O_{40}$ (Sigma-Aldrich 463922), 350 μM $Co(NO_3)_2 \cdot 6H_2O$ (Sigma-Aldrich 203106), and 20 mM $CH_3CO_2NH_4$ (Sigma-Aldrich A1542, as a buffer agent which will vaporize before size-selection). The mixed solution is atomized into nano-droplets suspended in clean air as a carrier gas through an Electrospray Aerosol Generator (TSI Inc. 3480). For the electrospray process, a silica capillary with an inner diameter of 40 μm is used to obtain a cone-jetting mechanism with a proper flow rate of carrier gas (~2 slpm) and 2 kV high voltage. A radioactive charge neutralizer (TSI 3077) is used to discharge the nano-droplet to avoid the splitting with the removal of water in the nano-droplet, leaving precipitated sNPs. The sNPs are then sent through a DMA (TSI 3085). The DMA selects particles with a prescribed mobility-equivalent diameter and a very narrow range. The DMA-selected nanoparticles are sent into an electrostatic precipitator for collection onto the target substrate.

Production of size-selected Fe-oNPs: Clean air (20 sccm) is set to pass through the container of ferrocene powder (Sigma-Aldrich F408) at room temperature. Another clean air (1 slpm) carries the vapor of ferrocene through an alumina tube in a furnace whose temperature is set to 700°C, the nucleated polydisperse Fe-oNPs are first charged using a radioactive charge neutralizer (TSI 3077) and then size-selected as above. The DMA-selected nanoparticles are sent into an electrostatic precipitator for collection onto the target substrate.

5.2. Substrate-based CVD growth of CNTs

To avoid or reduce possible aggregation, oNPs are first reduced in H_2 with the temperature slowly rising to 400°C to obtain mNPs. Then the temperature is raised quickly to 850°C (100 K/min). Ethanol vapor as the carbon feedstock is introduced immediately when the final temperature is reached (850°C) in an Ar carrier gas stream. The growth time is set to only 10 min. After growth, the carbon-rich environment is expelled by H_2, and the samples are cooled to room temperature.

5.3. Aerosol Characterization, AFM, HRTEM, EDS, and Raman Mapping

Aerosol size distributions of all NPs are analyzed using a Scanning Mobility Particle Spectrometer (**SMPS**), which consists of a combination of a **DMA** (TSI 3085) and a Condensation Particle Counter (**CPC**, TSI 3756). **AFM** is conducted on a Veeco Dimension Pro AFM on Peakforce mode. Both Transmission electron microscopy (**TEM**) and Energy-dispersive X-ray spectroscopy (**EDS**) elements mapping were conducted on a Thermo Scientific (FEI) Talos F200X G2 TEM operating at 200 kV. TEM images were acquired using a Ceta 16M CMOS camera. EDS was performed in Scanning transmission electron microscopy (**STEM**) mode with images acquired using the High angle annular dark field (**HAADF**) detector with EDX spectra/maps collected using the Super-X EDS detector system which consists of 4 windowless silicon drift detectors. Prior to TEM the NPs were dispersed onto Si_3N_4 TEM grids. **Raman mapping** is conducted in the RBM range, with 532, 638, and 785 nm lasers. The step size is set to 3 μm in both the x and y directions.

6. Patents

Pertaining UK patent has been filed with application number as 1917638.7., which is partially resulting from the work reported in this manuscript.

Author Contributions: Conceptualization, X.Z., B.G., M.D. and A.B.; methodology, X.Z., Y.D., B.G., M.D. and A.B.; validation, X.Z., Y.D., B.G., M.D. and A.B.; formal analysis, X.Z.; data curation, X.Z.; writing—original draft preparation, X.Z. and Y.D.; writing—review and editing, B.G., M.D. and A.B.; supervision, M.D. and A.B.; project administration, A.B.; funding acquisition, A.B, X.Z.. All authors have read and agreed to the published version of the manuscript.

Funding: This research was funded by EPSRC project 'Advanced Nanotube Application and Manufacturing (ANAM) Initiative' [grant numbers EP/M015211/1] and EPSRC Underpinning Multi-439 User Equipment Call [grant numbers EP/P030467/1], the National Key R&D Program of China (Grant 440 No. 2018YFA0208402) and

334 the National Natural Science Foundation of China (Grant Nos. 11634014 441 and 51820105002). The APC was
335 funded by Cambridge University's RCUK and/or COAF block grants.

336 **Acknowledgments:** The authors specially thanks Dr. Maksim Mezhericher, Dr. Weiya Zhou, Dr. Huaping Liu,
337 Prof. Kaihui Liu and Fengrui Rao for their useful guidance and information. The authors thank Mingzhao Wang,
338 Zhanyu Wang, Dr. Sarah Stevenson, Dr. Yanchun Wang, Liron Issman, Dr. Fiona Smail for their kind support
339 and useful discussion. The author also thanks Dr. Heather Greer, Dr. Adarsh Kaniyoor, and Jenny Mizen for
340 TEM and Raman experiment support.

341 **Conflicts of Interest:** The authors declare no conflict of interest. The funders had no role in the design of the
342 study; in the collection, analyses, or interpretation of data; in the writing of the manuscript, or in the decision to
343 publish the results.

References

345 1. Y. Li, H. Wang, C. Priest, S. Li, P. Xu, G. Wu, Advanced Electrocatalysis for Energy and Environmental
346   Sustainability via Water and Nitrogen Reactions, Adv. Mater. n/a(n/a)   2000381.
347 2. M.F.L. De Volder, S.H. Tawfick, R.H. Baughman, A.J. Hart, Carbon Nanotubes: Present and Future
348   Commercial Applications, Science 339(6119) (2013) 535-539.
349 3. X. Zhang, L. Song, L. Cai, X.Z. Tian, Q. Zhang, X.Y. Qi, W.B. Zhou, N. Zhang, F. Yang, Q.X. Fan, Y.C. Wang,
350   H.P. Liu, X.D. Bai, W.Y. Zhou, S.S. Xie, Optical visualization and polarized light absorption of the single-
351   wall carbon nanotube to verify intrinsic thermal applications, Light-Sci. Appl. 4 (2015) 8.
352 4. F. Yang, X. Wang, D. Zhang, J. Yang, D. Luo, Z. Xu, J. Wei, J.-Q. Wang, Z. Xu, F. Peng, X. Li, R. Li, Y. Li, M.
353   Li, X. Bai, F. Ding, Y. Li, Chirality-specific growth of single-walled carbon nanotubes on solid alloy
354   catalysts, Nature 510 (2014) 522.
355 5. X. Zhao, F. Yang, J. Chen, L. Ding, X. Liu, F. Yao, M. Li, D. Zhang, Z. Zhang, X. Liu, J. Yang, K. Liu, Y. Li,
356   Selective growth of chirality-enriched semiconducting carbon nanotubes by using bimetallic catalysts from
357   salt precursors, Nanoscale 10(15) (2018) 6922-6927.
358 6. S.M. Bachilo, L. Balzano, J.E. Herrera, F. Pompeo, D.E. Resasco, R.B. Weisman, Narrow (n,m)-Distribution
359   of Single-Walled Carbon Nanotubes Grown Using a Solid Supported Catalyst, Journal of the American
360   Chemical Society 125(37) (2003) 11186-11187.
361 7. S. Ahmad, Y. Liao, A. Hussain, Q. Zhang, E.-X. Ding, H. Jiang, E.I. Kauppinen, Systematic investigation of
362   the catalyst composition effects on single-walled carbon nanotubes synthesis in floating-catalyst CVD,
363   Carbon 149 (2019) 318-327.
364 8. X. Zhang, B. Graves, M.D. Volder, W. Yang, T. Johnson, B. Wen, W. Su, R. Nishida, S. Xie, A. Boies, High
365   Precision Solid Catalysts for Investigation of Carbon Nanotube Synthesis and Structure, Science Advances,
366   6:eabb6010 (2020) in press.
367 9. T.J. Johnson, M. Irwin, J.P.R. Symonds, J.S. Olfert, A.M. Boies, Measuring aerosol size distributions with
368   the aerodynamic aerosol classifier, Aerosol Science and Technology 52(6) (2018) 655-665.
369 10. D. Yuan, L. Ding, H. Chu, Y. Feng, T.P. McNicholas, J. Liu, Horizontally Aligned Single-Walled Carbon
370   Nanotube on Quartz from a Large Variety of Metal Catalysts, Nano Letters 8(8) (2008) 2576-2579.
371 11. L. Kang, S. Zhang, Q. Li, J. Zhang, Growth of Horizontal Semiconducting SWNT Arrays with Density
372   Higher than 100 tubes/μm using Ethanol/Methane Chemical Vapor Deposition, Journal of the American
373   Chemical Society 138(21) (2016) 6727-6730.
374 12. Y. Hu, L. Kang, Q. Zhao, H. Zhong, S. Zhang, L. Yang, Z. Wang, J. Lin, Q. Li, Z. Zhang, L. Peng, Z. Liu, J.
375   Zhang, Growth of high-density horizontally aligned SWNT arrays using Trojan catalysts, Nat. Commun.
376   6(1) (2015) 6099.
377 13. X. Zhang, F. Yang, D. Zhao, L. Cai, P. Luan, Q. Zhang, W. Zhou, N. Zhang, Q. Fan, Y. Wang, H. Liu, W.
378   Zhou, S. Xie, Temperature dependent Raman spectra of isolated suspended single-walled carbon
379   nanotubes, Nanoscale 6(8) (2014) 3949-3953.
380 14. D. Zhang, J. Yang, F. Yang, R. Li, M. Li, D. Ji, Y. Li, (n,m) Assignments and quantification for single-walled
381   carbon nanotubes on SiO2/Si substrates by resonant Raman spectroscopy, Nanoscale 7(24) (2015) 10719-
382   10727.
383 15. H. Kataura, Y. Kumazawa, Y. Maniwa, I. Umezu, S. Suzuki, Y. Ohtsuka, Y. Achiba, Optical properties of
384   single-wall carbon nanotubes, Synthetic Metals 103(1) (1999) 2555-2558.

385   16.   K.H. Liu, J. Deslippe, F.J. Xiao, R.B. Capaz, X.P. Hong, S. Aloni, A. Zettl, W.L. Wang, X.D. Bai, S.G. Louie,
386   E.G. Wang, F. Wang, An atlas of carbon nanotube optical transitions, Nat. Nanotechnol. 7(5) (2012) 325-
387   329.
388   17.   F. Ding, A.R. Harutyunyan, B.I. Yakobson, Dislocation theory of chirality-controlled nanotube growth, P
389   Natl Acad Sci USA 106(8) (2009) 2506-2509.
390   18.   V.I. Artyukhov, E.S. Penev, B.I. Yakobson, Why nanotubes grow chiral, Nat. Commun. 5 (2014) 4892.
391   19.   E.S. Penev, K.V. Bets, N. Gupta, B.I. Yakobson, Transient Kinetic Selectivity in Nanotubes Growth on Solid
392   Co-W Catalyst, Nano Letters 18(8) (2018) 5288-5293.
393   20.   K.V. Bets, E.S. Penev, B.I. Yakobson, Janus Segregation at the Carbon Nanotube–Catalyst Interface, ACS
394   Nano   (2019).
395   21.   S. Zhang, L. Kang, X. Wang, L. Tong, L. Yang, Z. Wang, K. Qi, S. Deng, Q. Li, X. Bai, F. Ding, J. Zhang,
396   Arrays of horizontal carbon nanotubes of controlled chirality grown using designed catalysts, Nature
397   advance online publication (2017).
398   22.   X. Wang, F. Ding, How a Solid Catalyst Determines the Chirality of the Single-Wall Carbon Nanotube
399   Grown on It, The Journal of Physical Chemistry Letters   (2019) 735-741.
400   23.   J. Li, Y. He, Y. Han, K. Liu, J. Wang, Q. Li, S. Fan, K. Jiang, Direct Identification of Metallic and
401   Semiconducting Single-Walled Carbon Nanotubes in Scanning Electron Microscopy, Nano Letters. (2012),
402   12, 8, 4095–4101
403   24.   M.Parhizkar, P. Reardon, J. Knowles, R. Browning, E.Stride, R. Pedley, T. Grego, M.Edirisinghe,
404   Performance of novel high throughput multi electrospray systems for forming of polymeric
405   micro/nanoparticles, Materials & Design. (2017), 126, 73-84
406